Deformation mechanisms in nacre

R.Z. Wang
Department of Chemical Engineering and Princeton Materials Institute, Princeton University, Princeton, New Jersey 08544

Z. Suo and A.G. Evans
Department of Mechanical and Aerospace Engineering and Princeton Materials Institute, Princeton University, Princeton, New Jersey 08544

N. Yao
Princeton Materials Institute, Princeton University, Princeton, New Jersey 08544

I.A. Aksay
Department of Chemical Engineering and Princeton Materials Institute, Princeton University, Princeton, New Jersey 08544

(Received 27 December 2000; accepted 4 June 2001)

Nacre (mother-of-pearl) from mollusc shells is a biologically formed lamellar ceramic. The inelastic deformation of this material has been experimentally examined, with a focus on understanding the underlying mechanisms. Slip along the lamellae tablet interface has been ascertained by testing in compression with the boundaries oriented at 45° to the loading axis. The steady-state shear resistance τ_{ss} has been determined and inelastic strain shown to be as high as 8%. The inelastic deformation was realized by massive interlamellae shearing. Testing in tension parallel to the tablets indicates inelastic strain of about 1%, occurring at a steady-state stress, $\sigma_{ss} \approx 110$ MPa. The strain was associated with the formation of multiple dilatation bands at the intertablet boundaries accompanied by interlamellae sliding. Nano-asperities on the aragonite tablets and their interposing topology provide the resistance to interfacial sliding and establish the level of the stress needed to attain the inelastic strain. Detailed mechanisms and their significance for the design of robust ceramics are discussed.

I. INTRODUCTION

Some biological materials exhibit structural robustness, despite the brittle nature of their constituents. Well known examples include bone, teeth, and mollusc shells.[1–3] Nacre (mother-of-pearl), the pearly internal layer of many mollusc shells, is addressed in this study. This material comprises about 95% aragonite (a mineral form of $CaCO_3$), with only a few percent of biological macromolecules: yet its work of fracture is about 3 orders of magnitude higher than monolithic ceramics,[4,5] and its strength is among the highest in shell structures.[6] A thorough understanding of the mechanisms underlying this robustness could inspire new ideas in material design and synthesis. The goal of this study, in conjunction with a companion theoretical analysis,[7] is to elucidate the basic mechanisms. As elaborated elsewhere,[8,9] good toughness is a necessary but not sufficient requirement for structural utility. The more basic prerequisite is a deformation mechanism that permits the material to exhibit inelastic strain when loaded in tension and shear. The basic idea is that (when sufficiently large, relative to elastic strains) this inelastic deformation allows the material to redistribute stress around strain concentration sites, thereby eliminating stress concentrations and, consequently, rendering the material "notch insensitive."[8,9] Absent this strain capacity, materials are susceptible to unpredictable failures from imperfections.

The prior research on nacre has mainly focused on the toughening behavior[4,10–15] as well as related attempts to synthesize tough laminates.[16–23] Toughness will not be addressed in this article. Instead, the focus will be on inelastic deformation and stress redistribution. While reported in the earliest research,[5,24] attempts to either characterize this response or establish the governing mechanisms have been minimal despite its critical role in robustness. This paper will experimentally characterize the inelasticity. The companion paper[7] assesses the mechanisms that govern it. The study has three elements. (i) Methods for precise measurement of the inelastic strains have been designed and implemented. (ii) The micromechanisms associated with the inelastic deformation have been characterized using a range of imaging methods. (iii) The topology of the mineral surfaces have

been characterized at the nanoscale and related to the mechanical response. These three elements are interrelated through a basic model.[7]

II. MATERIALS

Shells from California red abalone (*Haliotis rufescens*) and South Sea pearl oysters (*Pinctada maxima*) have been used. Abalone (AB) belongs to the class of gastropoda, while pearl oyster (PO) is from the class of biovalvia. They are among the biggest shells and represent two typical nacre structures: columnar and sheet (Fig. 1).[25] Both are lamellar. They comprise alternative layers of a relatively thick (0.2–0.9 μm) aragonite separated by nanoscale (approximately 20 nm) organic interlayers. The mineral layer exists as closely packed polygonal tablets (5–8-μm diameter), separated by a nanoscale organic interlayer, such that the cross section resembles a brick wall. In columnar nacre, the polygonal tablets from neighboring layers overlap in such a manner that the intertablet boundaries form tessellated bands perpendicular to the lamellae boundaries [Fig. 1(a)]. In sheet nacre, the intertablet boundaries are distributed randomly [Fig. 1(b)].

For the present study, adult shells were collected alive in Santa Barbara, CA, and Darwin, Australia. To minimize the detrimental effect of drying on the mechanical properties, they were cleaned and air-delivered in ice to Princeton, NJ, where the shells were stored in sea water at 4 °C until the experiments were conducted. The specimens were immersed in tap water during testing.

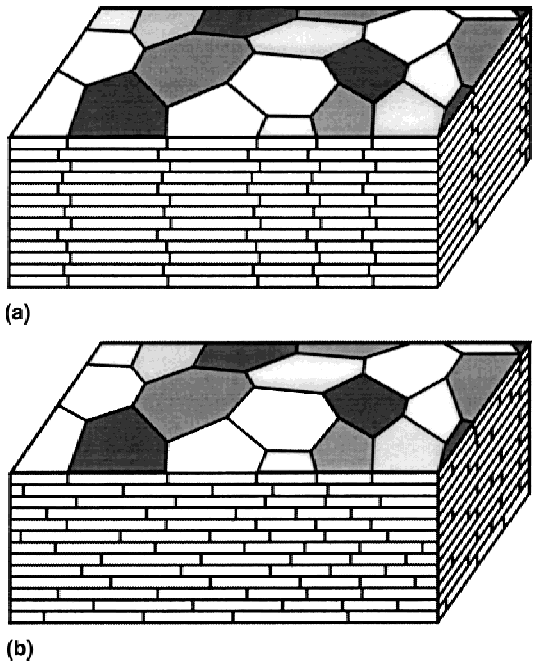

FIG. 1. Schematic illustrations of (a) columnar nacre/abalone shell and (b) sheet nacre/pearl oyster. Polygonal aragonite tablets are adhered into a lamellar structure by a thin organic interlayer. In columnar nacre, the intertablet boundaries are correlated into a tesselated arrangement.

III. MECHANICAL MEASUREMENTS

A. Approach

Four different measurement methods have been used to probe the overall mechanical response. Two of them involve flexure measurements performed on beams oriented such that the aragonite plates are aligned along the beam axis. (i) Three-point measurements were used to establish overall trends in inelastic deformation. (ii) Four-point tests were used to generate quantitative stress/strain information. For this purpose, strain gages were attached to the tensile and compressive faces, between the inner loading points: a deconvolution yields both the tensile and compressive stress/strain curves on each specimen.[26,27] (iii) Compression tests were performed on specimens cut with the lamellae boundaries at 45° to the load axis, to elicit shear deformation parallel to the plates. (iv) Finally, a notch flexure test was designed to explore the response of the material to strain concentrations.

The specimens were sectioned by using a water-cooled, low-speed diamond saw. One flexure category had the tensile surface parallel to the lamellae boundaries (*face-on* orientation) and the other perpendicular (*edge-on* orientation) (see Fig. 2 for illustration). They were mechanically ground on all cut surfaces and polished on the tensile and compressive surfaces (MULTIPOL 2 Precision Polishing Machine, Ultra Tec, Santa Ana, CA), using diamond pastes and then 0.05-μm alumina suspension. For compression testing, the lamellae boundaries

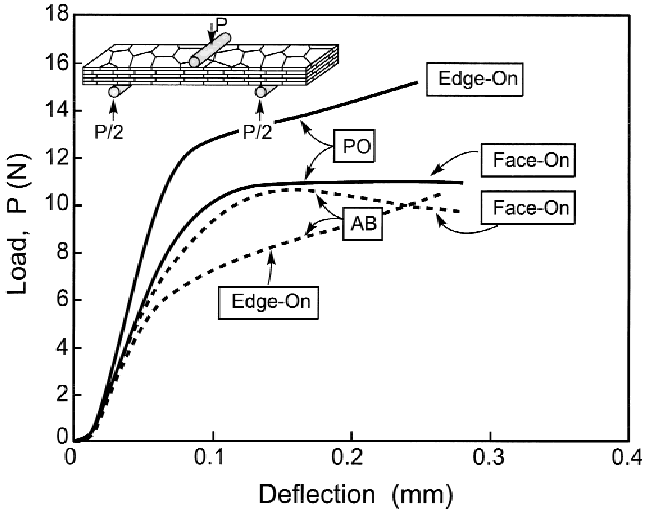

FIG. 2. Load–deflection curves upon three-point bending in the axial orientation. The insert indicates the face-on orientation, with the lamellar boundaries parallel to the tensile surface.

were oriented at 45° to the prism axis, perpendicular to the side surfaces (Fig. 3). The top and bottom surfaces, as well as two orthogonal side surfaces, were polished as above. All tests were conducted with a servohydraulic machine (Instron 8562, Canton, OH) at a speed of 0.5 mm/min. For the notch tests, a narrow slot was introduced by a diamond saw. The notched samples were then loaded either by three-point bending or by inserting a sharp wedge into the notch.

B. Overall trends

Three-point bending tests were performed on 20 specimens, each 0.5-mm depth, 2.5-mm wide, and 12-mm long on a span of 8 mm. Two linear variable differential transformer (LVDTs) (PLVX-1000, Sensotec, Columbus, OH) measured the relative displacement between the upper and the lower loading fixtures. Typical load/deflection curves are plotted in Fig. 2. All curves exhibited extensive inelastic deformation. The flexural modulus and strength calculated from these curves are listed in Table I.

Note that the elastic modulus and flexural strength are larger for pearl oyster nacre than for abalone nacre. Both edge-on and face-on orientations (Fig. 2) gave essentially the same modulus. However, in abalone nacre, the edge-on orientation exhibited lower strength, and the load at the onset of inelastic deformation was also lower (Fig. 2, Table I).

After testing, optical imaging provided a visualization of the inelastic zone, manifest as white tension lines (attributed to optical scattering centers created by the inelastic deformation mechanism, elaborated below). These lines were located in the central area of the tensile surface [Fig. 4(a)] perpendicular to the long axis, covering about one-third of the loading span. They were most dense opposite the central loading point. These findings confirm observations made by Currey[5] on another species of pearl oyster (*Pinctada margaritifera*).

C. Tensile and compressive stress/strain curves

Four-point bending tests were performed on five specimens, each 1.6-mm deep, 2.5-mm wide, and 16-mm long. The inner loading span was 6 mm, and the outer support span, 12 mm. Gages were used to measure the strains on both the tensile and the compressive surfaces (Omega Engineering, Stamford, CT). An example of the strains measured on both surfaces is plotted against applied load in Fig. 5(a). Note that the strains are substantially larger on the tensile surface.

Following the deconvolution that was originally suggested by Suo,[26] and was reproduced by Sugimura *et al.* in their Appendix,[27] the stress/strain curves in tension and compression have been obtained on the basis of the load and strains measured in four-point bending tests, as plotted in Fig. 5(b). The compressive curves are linear with a Young's modulus $E = 70$ GPa. The stress reached about 370 MPa before testing was discontinued.

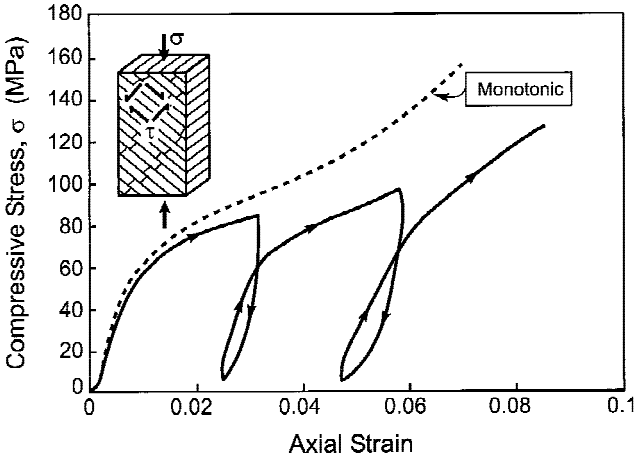

FIG. 3. Compression stress–strain curves for abalone nacre representing interlamellae shear, measured both in monotonic loading and with loading/unloading loops. The insert indicates that the lamellae boundaries are orientated at 45° to the loading axis.

TABLE I. Nominal strength and elastic modulus, E, of nacre, measured by three-point bending ($S/D = 16$).

Species	Orientation of tensile surface	Nominal strength (MPa)	E (GPa)
Abalone	Face-on	223 ± 7	69 ± 7
Abalone	Edge-on	194 ± 8	66 ± 2
Pearl oyster	Face-on	227 ± 13	77 ± 12
Pearl oyster	Edge-on	248 ± 14	81 ± 4

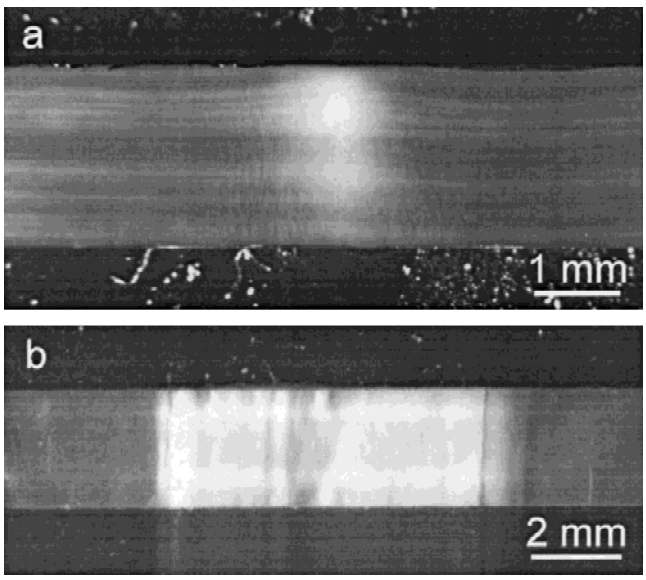

FIG. 4. White tension lines on the tensile surface of nacre specimens: (a) abalone, edge-on, three-point bending; (b) pearl oyster, face-on, four-point bending.

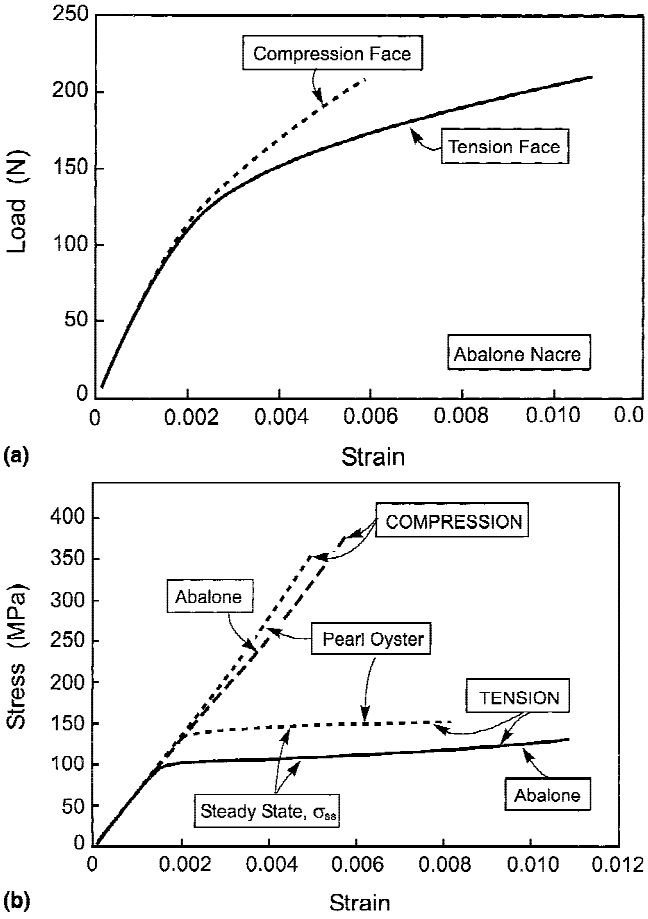

FIG. 5. (a) Load–strain curves for four-point bending in the axial orientation (face-on) and (b) deconvolated stress–strain curves in tension and compression.

Conversely, the tensile curves are highly nonlinear. After yielding, and following initial strain hardening, which occurs over a strain range of approximately 0.1%, the subsequent inelastic deformation occurs in "steady-state," at stress σ_{ss} (there is minimal strain hardening: tangent modulus < 3 GPa). This stress is about 105 MPa for abalone nacre and 140 MPa for pearl oyster nacre. The tensile ductility could not be measured, since the gages debonded at a strain of about 1.0%.

After testing, the white tension lines are again evident. On the tensile surface, they now distribute uniformly over the inner span [Fig. 4(b)]. On the side surfaces, they penetrate about half the specimen depth.

D. Shear stress/strain curves

The compression tests were performed on eight rectangular prismatic specimens, each 2.5-mm high with cross section 1.2 × 1.2 mm. Load was applied through a 3-mm tungsten carbide sphere, with a 1-mm-thick polished tungsten carbide insert to transfer the stress. LVDTs were mounted on the two opposite sides of the specimen to measure the displacement between the sphere and the base. A typical stress/strain curve, with loading/unloading loops (Fig. 3) reveals three salient features. (i) The failure strain is about 8%, much higher than in bending. (ii) The elastic modulus is only 8 GPa. (iii) The compressive strength is about 160 MPa, significantly lower than that parallel to the lamellae (>370 MPa). Following the elastic response, there are two stages of inelastic deformation. The first, which occurs at strains up to about 5%, exhibits minimal strain hardening (similar to that in tension). The second, at larger strains, has strong hardening. The specimens fail along the lamellae boundaries.

The unloading/reloading measurements reveal hysteresis (Fig. 3), indicative of internal friction, with an unloading modulus (17 GPa) slightly higher than that upon initial loading. When the displacement is fixed, stress relaxation occurs (for example, in 15 min, the stress drops by about 15 MPa) indicative of viscoplasticity, confirming an earlier report by Currey.[5]

E. Notch performance

The notched three-point bending samples are 2.5-mm deep, 1.6-mm wide, and 12-mm long on a span of 8 mm. Samples that are 8-mm deep, 3-mm wide, and 12-mm long are also notched. The latter were loaded by inserting a sharp wedge into the notch. The load/deflection curve exhibited nonlinearity prior to rupture, indicative of large scale yielding response. This response is visualized by optical imaging of the inelastic zone around the notch (Fig. 6). This zone has two notable features. It spreads out ahead of the notch, consistent with a dilatational (rather than shear) dominated mode of inelastic deformation, analogous to that found in transformation toughening.[28–30] It also contains several discrete, high-intensity bands suggestive of softening at large strain levels.[29] The implications are addressed below.

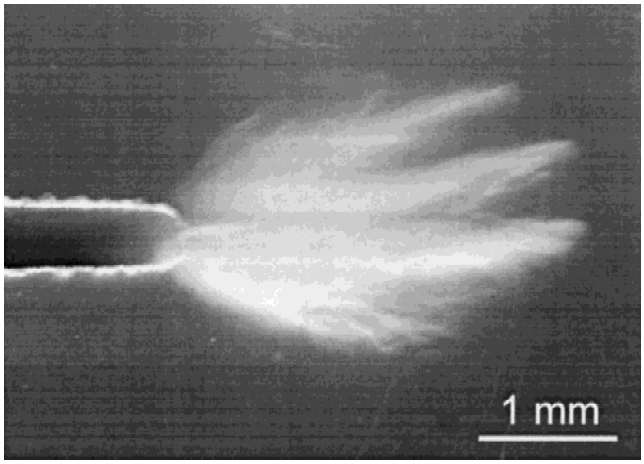

FIG. 6. White inelastic deformation zone at the notch tip for a face-on pearl oyster nacre specimen.

IV. CHARACTERIZATION

A. Methods

After testing, the samples were initially examined using a stereomicroscope (Leica MZ8, Wetzlar, Germany) and a metallurgical microscope (Leica MEF4M), followed by analysis of the structural details using scanning electron microscopy (Philip XL-30, Hillsboro, OR). For the latter, some samples were plasma-etched for 5 min to remove the surface layer damaged by polishing, followed by metal coating. Morphological changes on the deformed surfaces were characterized with an atomic force microscope (MultiMode SPM, Digital Instruments, Santa Barbara, CA).

B. Deformation bands

The optical contrast in the white tension lines described in Fig. 5 is found to arise from separations at tablet terminations, which cause the bands to dilate (Fig. 7). Accordingly, hereafter, they are referred to as "dilatation bands." When observed normal to the aragonite plates, the bands follow an irregular trajectory along the tablet boundaries [Figs. 7(b) and 7(d)]. When observed edge-on, they still appear at the intertablet boundaries but exhibit morphologies governed by the underlying lamellae architecture. In abalone nacre, they have a tessellated shape associated with the correlated architecture [Figs. 7(a), 7(c), and 7(e)]. In sheet nacre, the separations are randomly dispersed [Fig. 7(f)]. The separations within the bands are accommodated by sliding of the neighboring layers at the lamellae boundaries. The sliding displacements are evident from the distortions of fudicial marks present prior to testing [Fig. 7(e)].

In three-point bending, because the strain decreases with distance from the center, the effect of the strain on the separation between deformation bands can be ascertained. Furthest from the center, where the strain is lowest, the bands are widely separated and some of the intertablet boundaries are intact. Closer to the center, the band density progressively increases, until saturation

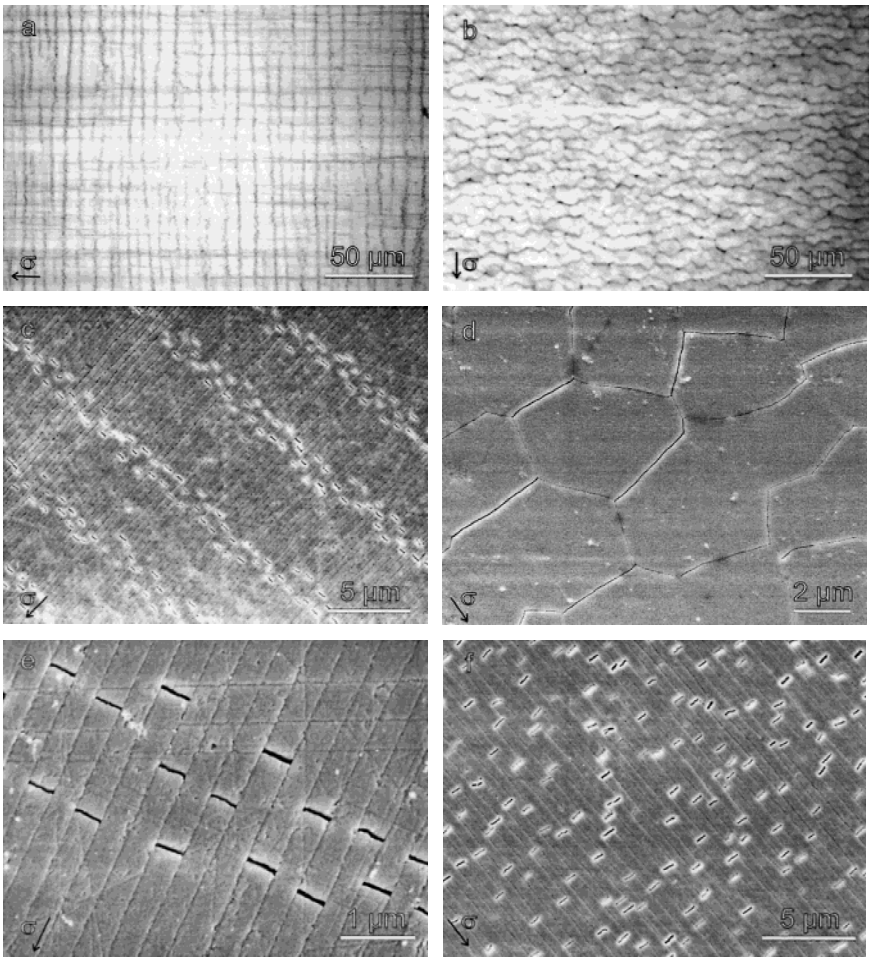

FIG. 7. White tension lines (or dilatation bands) at various magnifications: (a) abalone, edge-on, optical microscopy (OM), vertical bands; (b) pearl oyster, face-on, OM, horizontal bands; (c) abalone, edge-on, SEM showing four oblique dilatation bands; (d) pearl oyster, face-on, SEM, oblique bands; (e) abalone, edge-on, SEM showing one dilatation band from upper left to lower right; (f) pearl oyster, edge-on, SEM. Arrows indicate the orientation of tensile stress.

is reached (every boundary exhibits separations). The opening displacements of the separations are mostly in the range 20 to 50 nm but can be much larger at some locations.

The shearing response upon compression loading at 45° resulted in groups of uniformly distributed lines on the polished prismatic side surface, parallel to the lamellae boundaries [Fig. 8(a)]. These parallel lines are steps caused by lamellae slip along plate boundaries, as revealed by scanning electron microscopy (SEM) and atomic force microscopy (AFM) [Fig. 8(b)]. The height of each step varied from 10 to 30 nm. The steps were distributed uniformly on the surface, except in local nonslipping areas.

C. Topological characteristics

1. Surface morphology of aragonite tablets

Specimens were cleaved along lamellae boundaries, and the exposed surfaces were examined at high magnification using the AFM and SEM. The observations (Fig. 9) reveal nanoscale mineral islands about 30–100 nm in diameter and 10 nm in amplitude, separated by 60–120 nm, creating a peak and valley topography. These asperities are elongated in some areas of the abalone nacre (Fig. 10). They are smaller and more uniformly distributed in pearl oyster. SEM analysis of matching pairs of rupture surfaces indicates that the peaks and valleys interpose perfectly (Fig. 10).

Rodlike organic material is located in the valleys. It forms a network (Fig. 9), with ruptured ligaments observed in some locations.

2. Cross-section analysis

Polished and deformed edge-on specimens were plasma etched to remove the damage layer and imaged (Fig. 11). These images affirm that the asperities on the upper aragonite tablet interpose with those on the lower tablet (arrows in Fig. 11). The open areas between neighboring asperities were presumably occupied by the organic network (Fig. 9), prior to being preferentially etched by the plasma. An illustration on the nano-asperities at the lamellae boundaries and their interposing arrangement is sketched in Fig. 12.

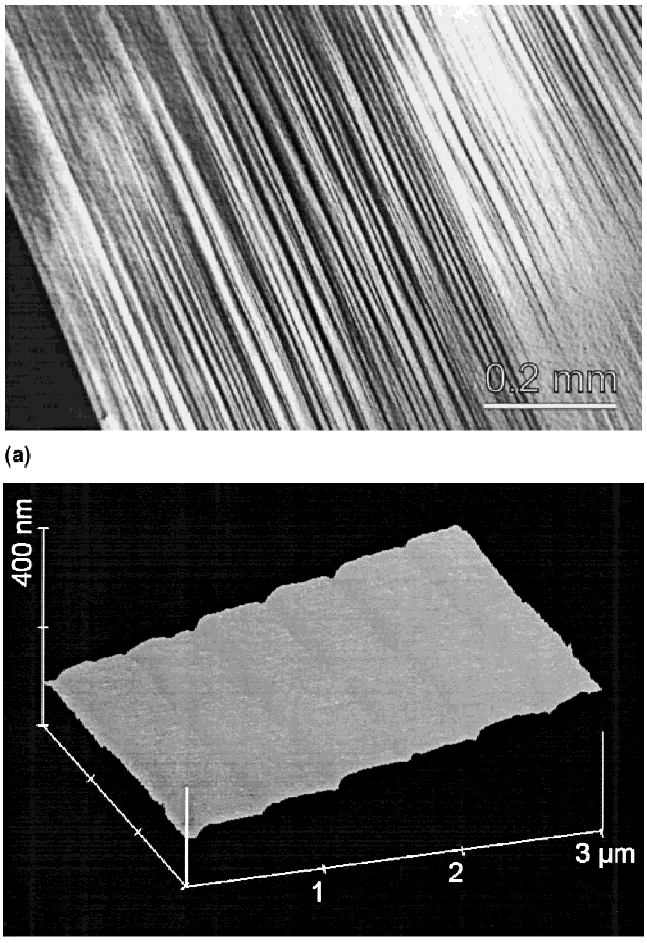

FIG. 8. (a) Uniformly distributed lines at low magnification on the prismatic side surface of a 45° compression abalone specimen. The straight line on the lower left is the edge view of the fractured surface and the lamellar boundary. (b) Atomic force microscopy of the lines showing slip steps at lamellae boundaries.

V. DISCUSSION

A. Mechanisms of inelastic deformation

The present measurements and observations affirm that, when loaded in compression at 45° to the interfaces, the aragonite plates shear over each other with a shear resistance, τ_{ss}. This shear is accompanied by dilatation, necessitated by a distribution of nano-asperities on the plate surfaces, which must translate past each other. It is hypothesized that the asperities are the principal source of the shear resistance, as elaborated in the companion paper.[7]

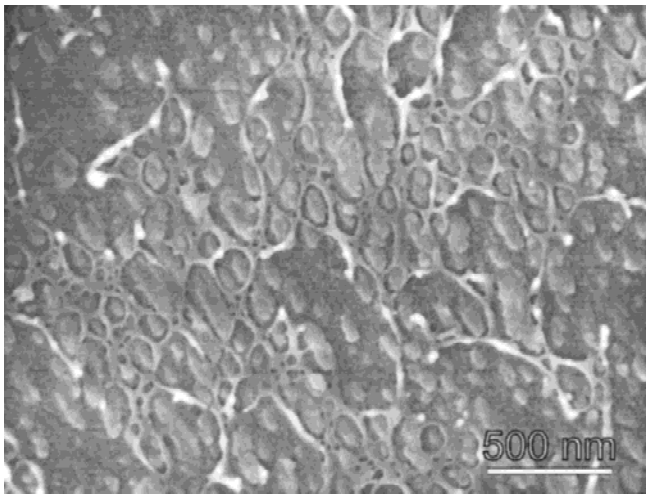

FIG. 9. Nano-asperities on the aragonite tablet surface of abalone nacre. The network surrounding them is the organic interlayer.

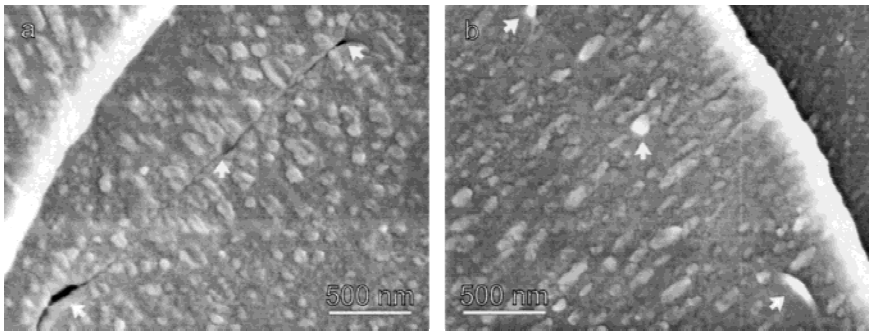

FIG. 10. Mirror images of opposing rupture surfaces of abalone nacre. Nano-asperities on the tablet surface at the left match those on the right. Arrows denote three matching locations for easy recognition.

Upon loading in tension, parallel to the plates, the interfaces at the plate edges rupture, causing separations to develop. These separations are able to open since the adjoining interfaces are susceptible to slip. The phenomenon is analogous to that found in fibrous oxides.[31,32] This slip response alleviates stress concentrations and enables the formation of dilatation bands, instead of a dominant brittle crack. Such bands are the source of the tensile inelasticity demonstrated in this study and, by inference, in *Pinctada margaritifera*.[5] The multiplicity of bands needed to realize the observed "ductility" is linked to the initial strain hardening,[7] enabled by asperity "climb." That is, as the asperities begin to translate and climb past each other, the system must dilate laterally, resulting in the development of transverse compression within the deformation bands that increases as the displacement proceeds. There is a balancing tension outside the bands. The elastic compression of the asperities in the slip zone induces hardening, which proceeds until the asperities juxtapose, whereupon the stress attains a maximum. Thereafter, the plates slip past each other, over the asperity peaks, at a steady-state shear resistance, τ_{ss}.

The separations open as the adjacent interfaces slip, whereupon the shear resistance, τ_{ss} governs the stress/strain responses through morphological quantities.[7] The specifics differ for the two types of nacre, discussed next. *For columnar nacre,* wherein the shear occurs in tessellated "dilatation bands," an explicit model has been developed.[7] In the hardening domain, prior to steady-state, the model predicts a stress/(plastic) strain [$\sigma(\epsilon_p)$] relation:

$$\frac{\sigma D^2}{EAL}(1+\nu L/D) \approx \left[\mu \sin(\pi S\epsilon_p/2l) + c_\mu \frac{D}{L}\sin(\pi S\epsilon_p/l)\right] \quad , \qquad (1)$$

where

$$c_\mu = 0.147 - 0.375\mu + 0.422\mu^2 \quad ,$$

with D the plate width, L the width of the dilatation band, $2l$ the asperity wavelength, A their amplitude, S the spacing between bands, and μ the friction coefficient. Upon insertion into Eq. (1) of the present measurements for the plate dimensions and the asperity characteristics, with the assumption that the friction coefficient is about zero,[7] the inelastic strains measured in the hardening domain are closely duplicated by this model. The same model also yields reasonable estimates of the steady-state stress, σ_{ss}, taken to be the maximum value of Eq. (1).[7] For sheet nacre, the principal difference is that the effective band width, L, is larger. It is stochastic in nature and governed by the spatial distribution of plates. Explicit predictions are not yet possible. However, the qualitative expectation from Eq. (1) is that larger L results in larger steady-state stress, as found experimentally [Fig. 5(b)].

As the separations continue to open, softening is predicted at large strains,[7] inconsistent with the present measurements, which imply a slight hardening [Fig. 5(b)]. This disparity suggests that there is a second (albeit small) contribution to the steady-state stress, probably involving shear deformation of the organic interlayer.

B. Role of the organic

The organic at the platelet interfaces appears to have two critical functions: (i) It must have sufficient plastic stretch to withstand the transverse tensile stresses induced between the dilatation bands. Consistent with this requirement, the organic has been observed to stretch into ligaments, subject to a measurable force–extension characteristic.[15] That is, the ligaments allow the nacre to remain intact and permit the dilation bands to evolve into steady state. (ii) The friction coefficient between sliding asperities must be influenced by the organic. The companion study[7] suggests that its effect is to lubricate the interface, leading to a friction coefficient of order zero.

Beyond these two functions, the shearing and stretching of the organic within the slipping domains appears to provide some resistance to deformation. This resistance

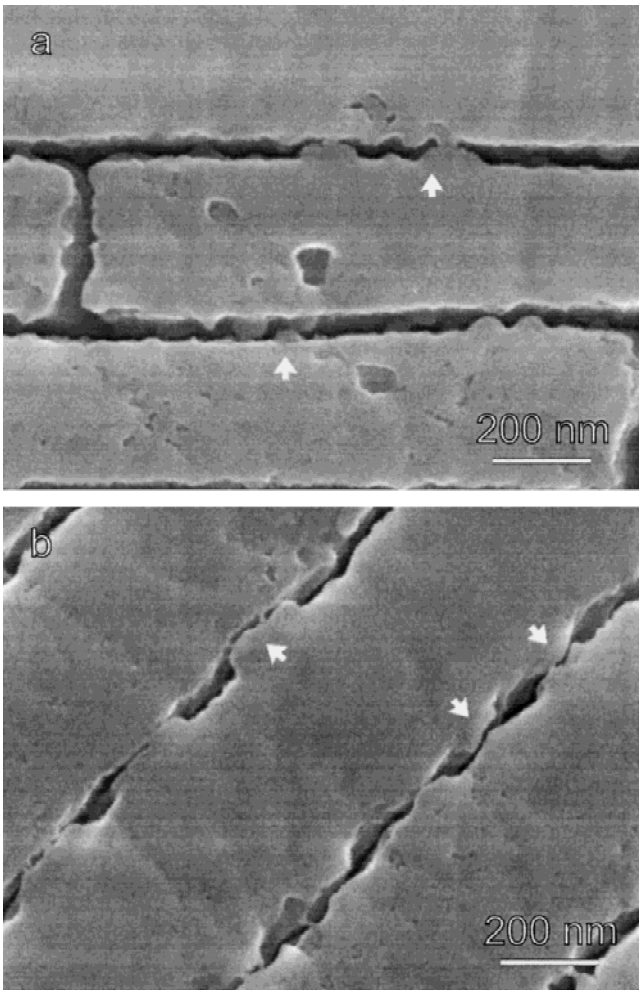

FIG. 11. Cross section of abalone nacre showing the detailed structure at the lamellae boundaries. Arrows highlight locations where the nano-asperities interpose.

would be time and rate dependent and is presumed to be the source of the stress relaxation noted in Sec. III. D and the reverse displacements when unloaded.[5] It is also likely to account for the hardening at large strains, found upon tensile and shear loading, as noted above.

C. Stress redistribution at notches

The observation of a large scale inelastic zone around a notch (Fig. 6) is a clear manifestation of the ability of nacre to redistribute stress and ameliorate stress concentrations. Related phenomena appear as plastic zones in metals, as well as dilatation zones in transformation toughened[28–30] and fibrous oxides.[8,9,31,32] For the latter, it has been shown by interferometry and by mechanical measurements that the inelastic zone eliminates stress concentrations and imparts structural integrity.[31,33]

That the shape of the inelastic zone is similar to that in transformation toughening[28] and in fibrous oxides[8] is consistent with a dilatational mode of inelastic deformation. Bands of highly concentrated strain within the inelastic zone have also been observed in transformation toughening.[29,30] They reflect a tendency for strain softening at large strains and are detrimental to the mechanical robustness. Such softening has not been found in the present stress/strain measurements but is likely to arise at larger strain levels, as the opening of the separations between plates becomes large.[7]

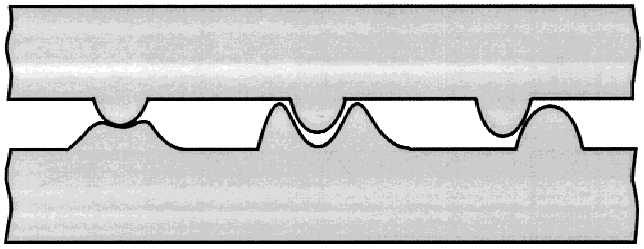

FIG. 12. Schematic illustration of the nano-asperities and three typical pairing topologies at neighboring aragonite plates.

VI. CONCLUSION

It has been established that nacre exhibits inelastic deformation in both shear and tension. The strain in shear parallel to aragonite plates is as high as 8% and at least 1% upon loading in tension axial to plates. In compression, it is linear elastic to failure.

Deformation in shear occurs by interlamellae slip and in the tension by the formation of multiple dilatation bands at intertablet boundaries accompanied by interlamellae sliding. The stress at which the inelastic deformation proceeds is governed by nano-sized mineral asperities on the surface of the aragonite tablets. Their interposing arrangements between neighboring lamellae dictate the sliding resistance subject to an initial strain hardening that facilitates the observed ductility.[7] The inelasticity imparts mechanical robustness by allowing redistribution of stress around strain concentration sites. Nacre thus presents a model structure for designing a robust laminated ceramic. Precise design of interfacial morphology at the nanoscale to control interlamellae slip appears to be the first step toward a ceramic laminate that exhibits tensile ductility. An organic interlayer that retains transverse integrity during slip provides a second requirement.

ACKNOWLEDGMENTS

This work was supported by the National Science Foundation (Grant DMR98-09483) and a grant from the Army Research Office under the Multidisciplinary University Research Initiative (Grant DAAH04-95-1-0102). We thank Dr. Daniel R. Mumm for assisting in the testing. We also thank Prof. Daniel E. Morse at UCSB and Dr. David Mills at Paspaley Pearling Company for kindly providing shell samples.

REFERENCES

1. S. Weiner and H.D. Wagner, Annu. Rev. Mater. Sci. **28,** 271 (1998).
2. S. Weiner and L. Addadi, J. Mater. Chem. **7,** 689 (1997).
3. *The Mechanical Properties of Biological Materials,* edited by J.D. Currey and J.F.V. Vincent (Cambridge University Press, Cambridge, United Kingdom, 1980).
4. A.P. Jackson, J.F.V. Vincent, and R.M. Turner, Proc. R. Soc. London, Ser. B **234,** 415 (1988).
5. J.D. Currey, Proc. R. Soc. London, Ser. B **196,** 443 (1977).
6. J.D. Currey, J. Zool. London **180,** 445 (1976).
7. A.G. Evans, R.Z. Wang, Z. Suo, I.A. Aksay, M.Y. He, and J.W. Hutchinson, J. Mater. Res. (2001, in press).
8. A.G. Evans and F.W. Zok, Solid State Phys. **47,** 177 (1994).
9. A.G. Evans, Acta Mater. **45,** 23 (1997).
10. A.P. Jackson, J.F.V. Vincent, and R.M. Turner, J. Mater. Sci. **25,** 3173 (1990).
11. J. Liu, M. Sarikaya, and I.A. Aksay, in *Hierarchically Structured Materials,* edited by E.B.I.A. Aksay, M. Sarikaya, and D.A. Tirrell (Materials Research Society, Pittsburgh, PA, 1992), pp. 9–17.
12. K.E. Gunnison, M. Sarikaya, J. Liu, and I.A. Aksay, *Hierarchically Structured Materials,* edited by E.B.I.A. Aksay, M. Sarikaya, and D.A. Tirrell (Materials Research Society, Pittsburgh, PA, 1992), pp. 171–183.
13. M. Sarikaya, K.E. Gunnison, M. Yasrebi, and I.A. Aksay, in *Materials Synthesis Utilizing Biological Processes,* edited by P.D.C.P.C. Rieke and M. Alper (Materials Research Society, Pittsburgh, PA, 1990), pp. 109–116.
14. R.Z. Wang, H.B. Wen, F.Z. Cui, H.B. Zhang, and H.D. Li, J. Mater. Sci. **30,** 2299 (1995).
15. B.L. Smith, T.E. Schaffer, M. Viani, J.B. Thompson, N.A. Frederick, J. Kindt, A. Belcher, G.D. Stucky, D.E. Morse, and P.K. Hansma, Nature **399,** 761 (1999).
16. W.J. Clegg, Acta Metall. Mater. **40,** 3085 (1992).
17. W.J. Clegg, K. Kendall, N. McN. Alford, T.W. Button, and J.D. Birchall, Nature **347,** 455 (1990).
18. A.P. Jackson, J.F.V. Vincent, and R.M. Turner, Composites Sci. Technol. **36,** 255 (1989).
19. M. Yasrebi, G.H. Kim, K.E. Gunnison, D.L. Milius, M. Sarikayan, and I.A. Aksay, in *Better Ceramics through Chemistry IV,* edited by B.J.J. Zelinski, C.J. Brinker, D.E. Clark, and D.R. Ulrich (Mater. Res. Soc. Symp. Proc. **180,** Pittsburgh, PA, 1990), pp. 625–635.
20. N. Almqvist, N.H. Thompson, B.L. Smith, G.D. Stucky, D.E. Morse, and P.K. Hansma, Mater. Sci. Eng., C **7,** 37 (1999).
21. A. Sellinger, P.M. Weiss, A. Nguyen, Y. Lu, R.A. Assink, W. Gong, and C.J. Brinker, Nature **394,** 256 (1998).
22. A.H. Heuer, D.J. Fink, V.J. Laraia, J.L. Arias, P.D. Calvert, K. Kendall, G.L. Messing, J. Blackwell, P.C. Rieke, D.H. Thompson, A.P. Wheeler, A. Veis, and A.I. Caplan, Science **255,** 1098 (1992).
23. I.A. Aksay, M. Trau, S. Manne, I. Honma, N. Yao, L. Zhou, P. Fenter, P.M. Eisenberger, and S.M. Gruner, Science **273,** 892 (1996).
24. J.D. Currey and J.D. Taylor, J. Zool. London **173,** 395 (1974).
25. S.W. Wise, Eclogae Geol. Helv. **63,** 775 (1970).
26. Z. Suo (unpublished research).
27. Y. Sugimura, J. Meyer, M.Y. He, H. Bart-Smith, J. Grenstedt, and A.G. Evans, Acta Metall. **45,** 5245 (1997).
28. R.M. McMeeking and A.G. Evans, J. Am. Ceram. Soc. **65,** 242 (1982).
29. P.E. Reyes-Morel and I-W. Chen, J. Am. Ceram. Soc. **71,** 343 (1988).
30. C-S. Yu, D.K. Shetty, M.C. Shaw, and D.B. Marshall, J. Am. Ceram. Soc. **75,** 2991 (1992).
31. J.B. Davis, D.B. Marshall, and P.E.D. Morgan, J. Eur. Ceram. Soc. **20,** 583 (2000).
32. C.G. Levi, J.Y. Yang, B.J. Dalgleish, F.W. Zok, and A.G. Evans, J. Am. Ceram. Soc. **81,** 2077 (1998).
33. J.C. McNulty, F.W. Zok, G.M. Genin, and A.G. Evans, J. Am. Ceram. Soc. **82,** 1217 (1999).